TESS Hunt for Young and Maturing Exoplanets (THYME). II. A 17 Myr Old Transiting Hot Jupiter in the Sco-Cen Association

Aaron C. Rizzuto[1,7] , Elisabeth R. Newton[2] , Andrew W. Mann[3] , Benjamin M. Tofflemire[1,7] , Andrew Vanderburg[1,8] ,
Adam L. Kraus[3] , Mackenna L. Wood[3] , Samuel N. Quinn[4] , George Zhou[4,9] , Pa Chia Thao[3,10] , Nicholas M. Law[3] ,
Carl Ziegler[5] , and César Briceño[6]

[1] Department of Astronomy, The University of Texas at Austin, Austin, TX 78712, USA; arizz@astro.as.utexas.edu
[2] Department of Physics and Astronomy, Dartmouth College, Hanover, NH 03755, USA
[3] Department of Physics and Astronomy, The University of North Carolina at Chapel Hill, Chapel Hill, NC 27599, USA
[4] Center for Astrophysics, Harvard & Smithsonian, 60 Garden St., Cambridge, MA 02138, USA
[5] Dunlap Institute for Astronomy and Astrophysics, University of Toronto, 50 St. George Street, Toronto, ON M5S 3H4, Canada
[6] Cerro Tololo Inter-American Observatory, Casilla 603, La Serena, Chile
Received 2020 April 13; revised 2020 May 15; accepted 2020 May 18; published 2020 June 22

Abstract

We present the discovery of a transiting hot Jupiter orbiting HIP 67522 ($T_{\rm eff} \sim 5650$ K; $M_* \sim 1.2 M_\odot$) in the 10–20 Myr old Sco-Cen OB association. We identified the transits in the TESS data using our custom notch filter planet search pipeline and characterize the system with additional photometry from Spitzer; spectroscopy from SOAR/Goodman, SALT/HRS, LCOGT/NRES, and SMARTS/CHIRON; and speckle imaging from SOAR/HRCam. We model the photometry as a periodic Gaussian process with transits to account for stellar variability and find an orbital period of $6.9596^{+0.000016}_{-0.000015}$ days and radius of $10.02^{+0.54}_{-0.53}$ $R_\oplus$. We also identify a single transit of an additional candidate planet with radius $8.01^{+0.75}_{-0.71}$ $R_\oplus$ that has an orbital period of $\gtrsim 23$ days. The validated planet HIP 67522b is currently the youngest transiting hot Jupiter discovered and is an ideal candidate for transmission spectroscopy and radial velocity follow-up studies, while also demonstrating that some young giant planets either form in situ at small orbital radii or else migrate promptly from formation sites farther out in the disk.

Unified Astronomy Thesaurus concepts: Exoplanet astronomy (486); Exoplanet evolution (491); Transits (1711); Young star clusters (1833); Star clusters (1567)

1. Introduction

The properties of exoplanets are likely a strong function of their age, reflecting the formation and evolutionary processes that shape them. Dynamical interactions and migration, whether through interaction with a circumstellar disk (Lubow & Ida 2010) or other planets in the system (e.g., Fabrycky & Tremaine 2007; Chatterjee et al. 2008), can alter orbital properties; photoevaporation from high-energy radiation or core heating can impact atmospheric properties (e.g., Ehrenreich et al. 2015; Gupta & Schlichting 2019); and the details of the greater star cluster environment can sculpt system architectures (Cai et al. 2017; van Elteren et al. 2019). The conditions and timescales under which each of these various mechanisms dominates are currently unclear, though the majority of evolution is expected to occur in the first few hundred million years following formation (Adams & Laughlin 2006; Mann et al. 2010; Lopez et al. 2012). Most observations of exoplanets are generally of mature, >1 Gyr old systems and as such only directly reflect the end-stage population.

Detection and characterization of young exoplanets provides one of the most direct avenues to mapping exoplanet evolution, and observations of exoplanets in clusters or associations of known age are particularly useful because they inherit the bulk properties such as age and metallicity of the host clusters to a level of precision not normally measurable for single field stars. Young exoplanets have been detected as part of direct imaging surveys (e.g., Bowler 2016; Nielsen et al. 2019), with radial

velocities (RVs) in young open clusters (e.g., Quinn et al. 2014), and with transits observed by the repurposed Kepler mission (K2; Howell et al. 2014), which observed several open clusters and associations (e.g., David et al. 2016, 2019; Mann et al. 2016a, 2017; Rizzuto et al. 2018).

The Transiting Exoplanet Survey Satellite (TESS; Ricker et al. 2014) mission provides the first opportunity for large-scale transit searches in young associations and young moving groups with ages <300 Myr. In particular, during the first year of observations, TESS observed the majority of the Scorpius–Centaurus OB association (Sco-Cen), a 10–20 Myr old, low-density comoving population of some ~10,000 members (Pecaut et al. 2012; Rizzuto et al. 2015). Sco-Cen is the nearest region of recently completed star formation to the Sun ($d \sim 140$ pc; de Zeeuw et al. 1999) and contains the vast majority of pre-main-sequence stars within the nearest 200 pc.

In this paper, we present the discovery of a hot, Jupiter-sized transiting exoplanet in the Sco-Cen association in the TESS Sector 11 data set. The host star is HIP 67522, an early G-type member of the Sco-Cen association originally identified kinematically by de Zeeuw et al. (1999). We also detect a single transit of a second companion in the system, with a radius that is closer to that of Saturn and an orbital period likely beyond the time baseline of a TESS observing sector. In Section 2 we present the TESS photometry, follow-up Spitzer transit photometry, and other ground-based follow-up. In Section 3 we derive stellar parameters and RVs and analyze the rotation of the host star. In Section 4 we reassess the membership of HIP 67522 in Sco-Cen in light of recent astrometric and photometric catalogs, and in Section 5 we present the results of transit model fits to the light curves from both TESS and Spitzer and address false positive scenarios. Finally, in

---
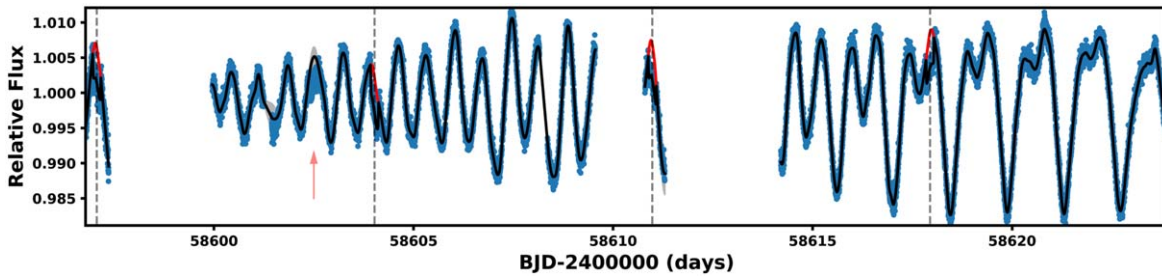
Figure 1. Light curve of HIP 67522 from TESS sector 11, corrected for systematics using the cotrending basis vector method described in Smith et al. (2012) (blue points) and the quaternion method of Vanderburg et al. (2019), and the GP model from the simultaneous transit and variability fit described in Section 5.1 (solid black line). Red sections showing the out-of-transit model, and vertical dashed lines indicate the four transits of the ∼7-day planet. Gray shaded regions indicate the uncertainty in the stellar rotation model and correspond to masked regions. The masked single transit of the HIP 67522 c candidate is marked by a red arrow.

Section 6 we discuss the system architecture, the implications for migration and formation of gas-giant exoplanets, and the potential for follow-up characterization.

2. Observations

2.1. TESS Photometry

TESS observed HIP 67522 during the 11th sector of observations between 2019 April 22 and 2019 May 21. HIP 67522 was preselected for short-cadence (2-minute) observations on the basis of its membership in the Sco-Cen association as part of our GI proposal G011280 (PI Rizzuto). The data were processed by the Science Processing and Operations Center (SPOC) pipeline at NASA Ames (Jenkins 2015; Jenkins et al. 2016), which performed pixel calibration, extracted light curves, deblended light from nearby objects, removed common-mode systematics with a cotrending basis vector analysis (Smith et al. 2012), high-pass-filtered the light curve, and searched for transits. Due to the high-amplitude rotational variability produced by spots (∼1%–2%; $P \sim 1.4$ days), which featured rotational structure on $\lesssim 1$ day timescales, the SPOC transit search pipeline registered a threshold crossing event consistent with our detection but rejected it as nonplanetary.

We applied the detrending and transit search algorithm of Rizzuto et al. (2017) to the SPOC light curve of HIP 67522, with a 0.5-day filtering window and transit durations of up to 5 hr. This method removes astrophysical variability with a notch filter, which fits a window of the light curve as a combination of an outlier-robust second-order polynomial and a trapezoidal notch. The inclusion of the notch allows detrending outside the notch without removal or overcorrection of transit-like signals. The window is then moved along each point in the light curve, detrending variability signals from the entire data set. In the case of HIP 67522, the rapid variability was not completely removed, as there is degeneracy between real transits and rotational signals of similar timescale. We improved the detection by taking into account the shape of potential transits with the notch filter. At each data point, we calculate the difference in Bayesian Information Criterion (BIC) for a model consisting of only the polynomial and a model including the notch. This difference will then be larger for transit-like shapes with rapid ingress and egress than for spot-induced variability on transit timescales. We searched for periodic transits in the time series of this BIC observable using the Box Least Squares (BLS) algorithm (Kovács et al. 2002). While the newer Transit Least Squares (TLS) algorithm (Hippke & Heller 2019) is generally an improvement over BLS for TESS data, this does not necessarily hold true for our specific case. The notch filter method we apply does not produce detrended light curves,

but rather filter response functions. The expected response is the convolution of the notch filter with itself (somewhat triangular), and as such TLS may not offer significant improvement in our case. Ideally we should search using the convolved notch filter shape, though we have opted not to do this for speed reasons.

A 13.92-day periodic signal was identified in the BLS power spectrum, corresponding to transits of approximately 0.5% depth and a distinctly transit-like shape (HIP 67522 b). Visual inspection of the two candidate transits confirms that their shape is inconsistent with any other rotational variability profiles in the light curve of HIP 67522. We also identify an additional single transit of a second planet candidate in the light curve (see Section 5.2).

The TESS sector 11 data from the SPOC pipeline feature a large gap between the two TESS orbits caused by the occurrence of a large scattered light event. We reinspected the original postage stamps of this section of data and a similar discarded section at the beginning of sector 11. We removed instrumental systematics following the quaternion methodology of Vanderburg et al. (2019) and identify two additional transits of HIP 67522 b, revealing the true period to be 6.96 days. Figure 1 shows the SPOC light curve with the additional sections, as well as the epochs of the transits.

2.2. Spitzer IRAC Photometry

Following the detection of transits with TESS, we scheduled observations of a transit of HIP 67522b with the Spitzer Space Telescope. The observations were taken on 2019 December 9 UTC (program ID 14011, PI Newton) using the Infrared Array Camera in channel 2 at 4.5 μm (IRAC; Fazio et al. 2004). We took a total of 19,968 frames in the 32 × 32 subarray, each of 1.9 s, spanning a total of 11.2 hr. As suggested by Ingalls et al. (2012, 2016), we placed the target on the location of peak sensitivity in IRAC channel 2 and used the "peak-up" pointing mode to keep the position of the star fixed to within 0.5 pixels using the Spitzer Pointing Calibration Reference Sensor.

We processed the Spitzer images to produce light curves using the Photometry for Orbits, Eccentricities, and Transits pipeline (POET;[11] Campo et al. 2011; Stevenson et al. 2012). This process included flagging and masking of bad pixels and calculation of Barycentric Julian Dates for each frame. The centroid position of the star in each image was then estimated by fitting a two-dimensional, elliptical Gaussian to the point-spread function in a 15-pixel square centered on the target position (Stevenson et al. 2010). Raw photometry was produced using simple aperture photometry using apertures

---

[11] https://github.com/kevin218/POET

Table 1
Spitzer IRAC CH2 Bliss Model Fit Parameters for HIP 67522b

Parameter	HIP 67522b
T_0 (BJD)	$2458826.72742^{+0.00028}_{-0.00027}$
T_{14} (days)	0.01444 ± 0.00011
$R_P/R_\star$	0.0683 ± 0.0011
$T_{12/34}$ (days)	0.00097 ± 0.00011
System flux (μJy)	88208^{+2271}_{-2198}
Sine amplitude	$14.4^{+3.9}_{-4.3}$
Sine period (days)	$3.29^{+0.47}_{-0.50}$
Sine phase offset	$0.17^{+0.13}_{-0.12}$
Constant	$15.5^{+4.3}_{-3.9}$
TESS T_0[a] (BJD)	$2,458,826.741 \pm 0.0152$

Note.
[a] Taken from the transit fit to only the TESS mission light curve in Table 4.

Figure 2. BLISS map of the relative subpixel sensitivity.

Figure 3. Top: Spitzer IRAC channel 2 data of a transit of HIP 67522b. Blue points are the raw Spitzer light curve, black circles are the same data binned into 70 bins, and the red line is the best-fit BLISS model consisting of a sine ramp, transit, and subpixel sensitivity map. The red vertical line indicates the best-fit center of transit, and the vertical black dashed lines indicate the 2σ range of the expected transit center based on the TESS detection. Bottom: residuals after subtraction of the best-fit model.

with diameters of 3.0, 3.25, 3.5, 3.75, and 4.0 pixels, each with a sky annulus of 9–15 pixels. Upon inspection of the resulting raw light curves, we saw no significant difference based on the choice of aperture size, and so the 3.5-pixel aperture was used for the rest of the analysis.

The Spitzer detectors have significant intrapixel sensitivity variations that can produce time-dependent variability in the photometry of a target star as the centroid position of the star image moves on the detector (Ingalls et al. 2012). To correct for this source of potential systematics, we applied the BiLinearly Interpolated Subpixel Sensitivity (BLISS) mapping technique of Stevenson et al. (2012), which was provided as an optional part of the POET pipeline. BLISS fits a model to the transit of an exoplanet that consists of a series of time-dependent functions, including a ramp and a transit model, and a spatially dependent model that maps sensitivity to centroid position on the detector. There are several choices of ramp models that can be used to model the out-of-transit variability, and usually a linear or quadratic is used for IRAC channel 2. We found that there was significant variability in the light curve of HIP 67522 that was not well fit by those standard choices of model. This is most likely due to the presence of both a detector ramp and stellar rotational variability in the light curve. We instead found that a sine function matched the data well. We modeled the planet transit as a symmetric eclipse without limb darkening, as the purpose of this model was to remove time-dependent systematics and leave a spatially dependent sensitivity map. The time-dependent component of the model consisted of the midtransit time (T_0), transit duration including ingress and egress (T_{14}), ingress and egress times ($T_{12/34}$), planet-to-star radius ratio ($R_P/R_\star$), system flux, ramp period, ramp phase, ramp amplitude, and ramp constant offset. These parameters were explored with a Markov Chain Monte Carlo (MCMC) process, using four walkers with 10,0000 steps and a burn-in region of 50,000 steps. At each step, the BLISS map was computed after subtraction of the time-dependent model components.

Table 1 lists the best-fit parameters and 68% credible intervals on the posteriors, Figure 2 shows the intrapixel sensitivity BLISS map, and Figure 3 shows the Spitzer light curve of HIP 67522b, the best-fit BLISS model and residuals, and the expected position of the transit center based on the TESS detection. We find that the center of the transit in the Spitzer data is within 2σ of the expected position based on our model of the TESS light-curve data (see Section 5.1). We then
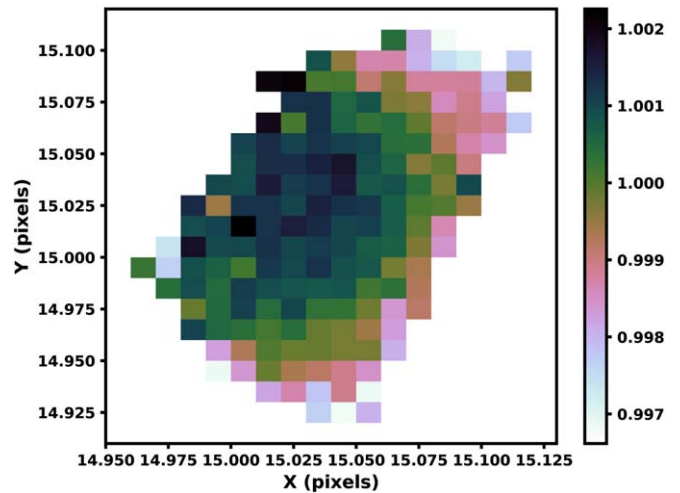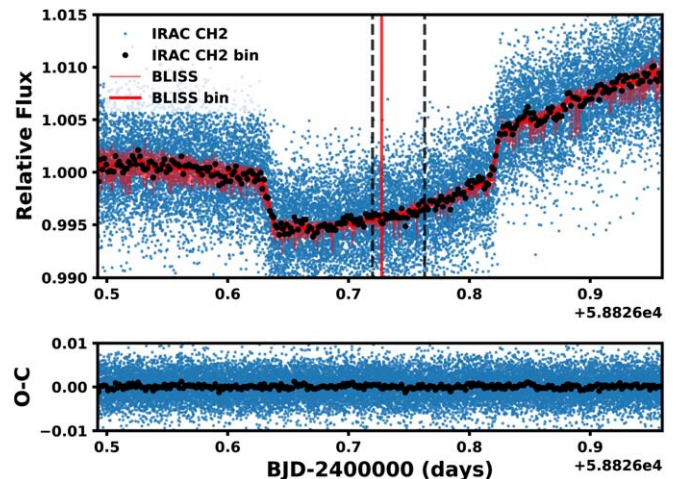
subtract the spatial component of the BLISS model, namely, the subpixel sensitivity map, yielding a light curve corrected for positional systematics, which we use in a combined transit fit with the TESS data (Section 5.1).

2.3. Limits on Companions from Imaging and Gaia

To rule out any unresolved companions that might impact our interpretation of the transit, we obtained speckle imaging using the High-Resolution Camera (HRCam) at the 4.1 m Southern Astrophysical Research (SOAR) telescope located in Cerro Pachón, Chile. We obtained four data cubes, two with 2×2 binning and two without binning. All images were taken in the I band and reduced according to Ziegler et al. (2020). We show the contrast limits in Figure 4. The SOAR speckle imaging has an outer working angle of $\sim 3''$. No companion was detected out to the outer working angle of SOAR speckle ($3''$); wider companions than this should be detected by Gaia and included in the second data release (Lindegren et al. 2018).
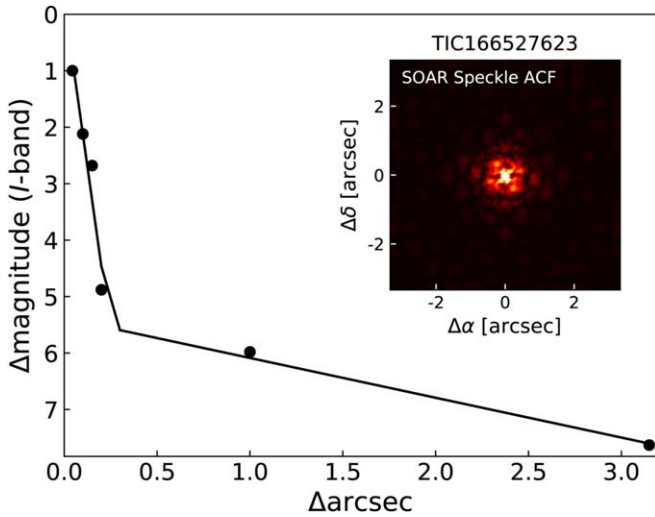
Figure 4. Detection limits from SOAR speckle imaging for HIP 67522.

Our null detection from speckle interferometry is consistent with the deeper limits set by the lack of Gaia excess noise, as indicated by the renormalized unit weight error (RUWE; Lindegren et al. 2018).[12] HIP 67522 has RUWE = 0.91, consistent with the distribution of values seen for single stars. Based on a calibration of the companion parameter space that would induce excess noise (Rizzuto et al. 2018; A. L. Kraus et al. 2020, in preparation), this corresponds to contrast limits of $\Delta G \sim 0$ mag at $\rho = 30$ mas, $\Delta G \sim 4$ mag at $\rho = 80$ mas, and $\Delta G \sim 5$ mag at $\rho \geqslant 200$ mas. The evolutionary models of Baraffe et al. (2015) would imply corresponding physical limits for equal-mass companions at $\rho \sim 4$ au, $M \sim 0.5 M_\odot$ at $\rho \sim 10$ au, and $M \sim 0.3 M_\odot$ at $\rho > 25$ au.

The Gaia DR2 catalog (Lindegren et al. 2018) also does not report any comoving, codistant neighbors within $\rho < 300'$ ($\rho < 38{,}000$ au) from HIP 67522. At separations beyond this limit, any neighbor would be more likely to be an unbound member of Sco-Cen, rather than a bound binary companion (e.g., Kraus & Hillenbrand 2008), so we conclude that there are no wide companions to HIP 67522 above the Gaia catalog's completeness limit. Ziegler et al. (2018) and Brandeker & Cataldi (2019) have mapped the completeness limit close to bright stars to be $\Delta G \sim 6$ mag at $\rho = 2''$, $\Delta G \sim 8$ mag at $\rho = 3''$, and $\Delta G \sim 10$ mag at $\rho = 6''$. The evolutionary models of Baraffe et al. (2015) would imply corresponding physical limits of $M \sim 0.15 M_\odot$ at $\rho = 255$ au, $M \sim 0.06 M_\odot$ at $\rho = 383$ au, and $M \sim 0.02 M_\odot$ at $\rho = 766$ au. At wider separations, the completeness limit of the Gaia catalog ($G \sim 20.5$ mag at moderate galactic latitudes; Lindegren et al. 2018) corresponds to an absence of any companions down to a limit of $M \sim 0.015 M_\odot$.

2.4. Spectroscopy

HIP 67522 was observed multiple times with a range of spectrographs, starting in 2004, and mostly during 2019. In order to derive the stellar properties, we obtained low-resolution spectra with the SOAR/Goodman spectrograph. To construct the RV curves needed to confirm and further characterize the system, we obtained high-resolution multiepoch spectroscopy with SALT/ HRS, SMARTS/CHIRON, LCO/NRES, and archival data from

Table 2
Radial Velocity and Projected Rotational Velocity Measurements of Host Star HIP 67522

Instrument	BJD	RV km s^{-1}
LCOGT:NRES	58,680.52486	8.3 ± 0.5
LCOGT:NRES	58,682.53411	7.4 ± 0.4
LCOGT:NRES	58,684.47585	8.4 ± 0.9
LCOGT:NRES	58,685.47600	7.7 ± 0.6
LCOGT:NRES	58,692.47785	7.9 ± 1.1
LCOGT:NRES	58,695.56019	8.1 ± 0.8
SALT:HRS	58,690.30040	$7.15 \pm 0.19.0$
SALT:HRS	58,693.29021	$7.40 \pm 0.18.0$
SALT:HRS	58,700.28479	$7.42 \pm 0.07.0$
SMARTS:CHIRON	58,694.61145	7.26 ± 0.17
SMARTS:CHIRON	58,695.59035	7.64 ± 0.26
SMARTS:CHIRON	58,698.55321	7.72 ± 0.18
SMARTS:CHIRON	58,700.53088	7.93 ± 0.22
SMARTS:CHIRON	58,701.47900	7.59 ± 0.19
SMARTS:CHIRON	58,702.54990	7.40 ± 0.14
SMARTS:CHIRON	58,704.48051	7.95 ± 0.16
SMARTS:CHIRON	58,705.53525	7.60 ± 0.16
SMARTS:CHIRON	58,706.50439	7.53 ± 0.2
SMARTS:CHIRON	58,707.46434	7.60 ± 0.17
SMARTS:CHIRON	58,708.48880	7.19 ± 0.27
ESO 2.2 m:FEROS	53,075.78544	8.58 ± 0.07
Error weighted mean RV		7.78 ± 0.54
SALT $v \sin i$		54.9 ± 0.1
LCOGT:NRES $v \sin i$		54.9 ± 0.4
SMARTS:CHIRON $v \sin i$		51.9 ± 0.3
ESO 2.2 m:FEROS $v \sin i$		54.2 ± 0.02
Error weighted mean $v \sin i$		54.2 ± 0.7

La Silla 2.2 m/FEROS spectrographs. Below we describe these observations, and Table 2 lists the instruments used, observation dates, and resulting RV measurements.

2.4.1. SOAR/Goodman

HIP 67522 was observed with the Goodman High-throughput Spectrograph (Clemens et al. 2004) on the Southern Astrophysical Research (SOAR) 4.1 m telescope located at Cerro Pachón, Chile. On 2019 August 3 (UT) and under clear (photometric) conditions, we obtained five spectra of HIP 67522, each with an exposure time of 15 s. We took all exposures using the red camera, the 400 line mm^{-1} grating in the M2 setup, and the $0.''46$ slit rotated to the parallactic angle, which yielded a resolution of $R \simeq 1850$ spanning 5000–9000 Å.

Using custom scripts, we performed bias subtraction, flat-fielding, optimal extraction of the target spectrum, and mapping pixels to wavelengths using a fourth-order polynomial derived from the HgArNe lamp spectra. We then stacked the five extracted spectra using the robust weighted mean (for outlier removal). The stacked spectrum had a signal-to-noise ratio >100 over the full wavelength range (excluding areas of strong telluric contamination). While we took no spectrophotometric standards during the night, we instead corrected instrument throughput with wavelength using standards from an earlier night.

2.4.2. SALT/HRS

HIP 67522 was observed with the Southern African Large Telescope High Resolution Spectrograph (SALT:HRS; Buckley et al. 2006; Crause et al. 2014) on three nights (2019 July 25 and

28 and August 4). On each visit, HIP 67522 was observed with 350 μm fibers in high-resolution mode for 320 s. The HRS data were reduced using the MIDAS pipeline (Kniazev et al. 2016), which performs flat-fielding, bias subtraction, and wavelength calibration with lamp exposures. The resulting spectral resolution is $R \sim 46,000$.

2.4.3. LCOGT/NRES

HIP 67522 was observed on six occasions with the Los Cumbres Observatory Global Telescope (LCOGT) Network of Robotic Echelle Spectrographs (NRES; Siverd et al. 2018). These are a network of $R = 53,000$ fiber-fed spectrographs on 1 m telescopes operating in the optical (380–860 nm). These observations spanned 2019 July 16–31. Each visit consisted of a 2400 s exposure, which provided a spectrum with a signal-to-noise ratio of 30–50. The raw data were automatically reduced with the NRES pipeline. This included bias subtraction, performing order trace and optimal extraction of the spectra, cosmic-ray rejection, and wavelength calibration.

2.4.4. SMARTS/CHIRON

HIP 67522 was observed on 11 nights spanning 2019 July 30–August 8. We obtained 11 epochs of spectroscopic observations with the CHIRON spectrograph on the 1.5 m SMARTS telescope spanning 2019 July 30–August 8. CHIRON is a high-resolution echelle spectrograph fed by an image slicer and a fiber bundle, located at Cerro Tololo Inter-American Observatory (CTIO), Chile. The spectra have a resolution of $R = 80,000$ with a wavelength coverage of 4100–8700 Å (Tokovinin et al. 2013). The wavelength solution is provided by bracketing Thorium-Argon cathode-ray lamp observations. The spectra are extracted with the official CHIRON pipeline. The velocities are derived by cross-correlations against synthetic templates from the ATLAS9 atmospheric library (Castelli & Kurucz 2004).

2.4.5. La Silla 2.2 m/FEROS

HIP 67522 was observed on 2004 March 11 with ESO's Fibre-fed, Extended Range, Echelle Spectrograph (FEROS) on the La Silla 2.2 m telescope (Kaufer et al. 1999). These observations were taken as part of Program 072.D-0021(B) (PI Nitschelm) in a search for spectroscopic binaries in Sco-Cen. FEROS provides spectra of $R \sim 48,000$ covering 350–920 nm, which are reduced with the MIDAS pipeline. This included flat-fielding, bad pixel masking, sky subtraction, and wavelength calibration.

2.5. Literature Photometry and Astrometry

To characterize the properties of the host star, we drew photometry and astrometry from the wider literature for HIP 67522. We took proper motions, parallax, and optical G, RP, and BP photometry from the Gaia second data release (DR2; Lindegren et al. 2018). We also drew V_T and B_T photometry from Tycho 2 (Perryman & ESA 1997); B and g' photometry from the American Association of Variable Stars Observers All-Sky Survey (APASS; Henden et al. 2012); near-infrared J, H, and K_s photometry from the Two Micron All Sky Survey (2MASS; Skrutskie et al. 2006); and mid-infrared $W_1 - W_4$ photometry from the Wide-Field Infrared Survey Explorer (AllWISE; Wright et al. 2010; Mainzer et al. 2011).
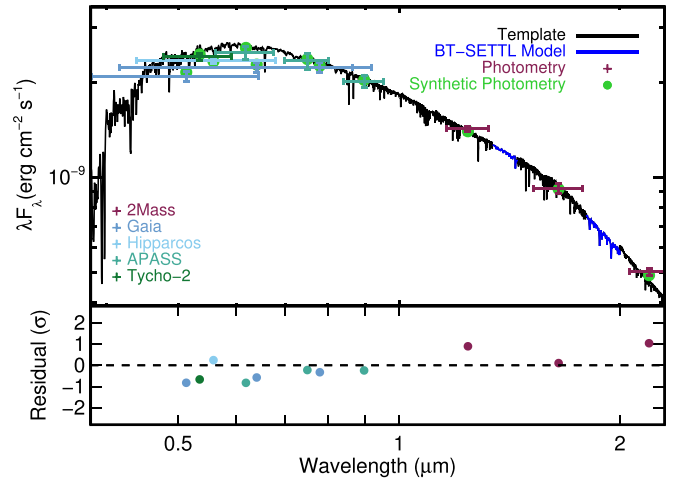
Figure 5. Best-fit spectral template and Goodman spectrum (black) compared to the photometry of HIP 67522. Blue regions are BT-SETTL models, used to fill in gaps or regions of high telluric contamination. Literature photometry is colored by the source, with horizontal errors corresponding to the filter width and vertical errors corresponding to the measurement errors. Corresponding synthetic photometry is shown as green circles. The bottom panel shows the residuals in terms of standard deviations from the fit, matching the color of the photometry source.

3. Measurements

3.1. Stellar Parameters

Luminosity, Radius, and Effective Temperature: We fit the spectral energy distribution of HIP 67522 using the available photometry, the Goodman optical spectrum, and spectral templates of nearby (unreddened) young stars. More details of our method can be found in Mann et al. (2015), with additional details on how we fit for reddening in Mann et al. (2016b), both of which we summarize here. We compared the photometry described in Section 2.5 to synthetic magnitudes derived from the combination of our SOAR spectrum, the template spectra, and Phoenix BT-SETTL models (Allard et al. 2011) to cover gaps in the spectra (e.g., beyond 2.5 μm), using appropriate filter profiles and zero-points (e.g., Cohen et al. 2003; Bessell & Murphy 2012; Mann & von Braun 2015; Maíz Apellániz & Weiler 2018). Errors in the photometry account for measurement errors, uncertainty in the zero-points and filter profiles (where available), and an estimate of stellar variability (0.02 mag in the optical). Photometry was weighted by these uncertainties in the comparison. We included reddening as an additional free parameter (assuming $A(V)/E(B - V) = 3.1$), which is added to the template and model spectra to better match the observed quantities. Tests against external spectra suggest that our flux calibration is only good to $\simeq 10\%$, so we included two additional free parameters to model errors in the spectral shape.

In addition to $E(B - V)$, our χ^2 comparison provided an estimate of $T_{\rm eff}$ from the the best-fit atmosphere model, L_* from the integral of the calibrated spectrum and Gaia DR2 distance, and R_* from the Stefan–Boltzmann relation. For HIP 67522, our final values were $T_{\rm eff} = 5650 \pm 75$ K, $L_* = 1.75 \pm 0.09 L_\odot$, and $R_* = 1.392 \pm 0.055 R_\odot$, with a low extinction of $E(B - V) = 0.02^{+0.03}_{-0.02}$. The final calibrated and combined spectrum is shown in Figure 5.

Age and Stellar Mass: we fit the effective temperature and luminosity of HIP 67522 measured in Section 3.1 to the PARSEC 1.2 s isochrones of Bressan et al. (2012) and the BHAC15

isochrones of Baraffe et al. (2015) to determine an age and mass estimate for the host star. We did not adopt an age a priori, as the age of stars in different regions of the Sco-Cen association can range from 5 to 20 Myr (Pecaut & Mamajek 2016). We fit a model with age and mass as parameters. We interpolated the isochrone grid and explored the posterior using the MCMC framework emcee (Foreman-Mackey et al. 2013). In our fit, we assumed solar metallicity for HIP 67522, which is consistent with estimates for the young regions around Sco-Cen (James et al. 2006).

We find a best-fit age of $\tau = 17.0^{+2.7}_{-1.5}$ Myr for the BHAC15 models and $\tau = 16.6 \pm 2.2$ Myr for the PARSEC models. Both models produced similar masses of $M = 1.2 \pm 0.05\,M_{\odot}$. In combination with our stellar radius measurement, this gives a stellar density $\rho_{\star}/\rho_{\odot} = 0.46 \pm 0.06$, which we adopt as a prior for the transit analysis described below.

3.2. Radial Velocities

To determine RVs, we compute spectral-line broadening functions (BFs; Rucinski 1992; Tofflemire et al. 2019). BFs were computed using a 6000 K synthetic template (Husser et al. 2013), which was found to provide the best order-to-order RV stability from a grid of templates sampled in steps of 100 K. Adjacent templates within 300 K provided consistent RV measurements. In each epoch we find that the BF is rotationally broadened but single-peaked, indicating the contribution from a single star.

To measure RVs, the BF is computed for each echelle order and combined, weighted by its S/N, and fit with a rotationally broadened stellar line profile. Uncertainties on these measurements are calculated as the standard deviations of the profile fits from BFs combined from three independent subsets of the echelle orders. Some epochs consisted of three consecutive integrations, for which the quoted RV and uncertainty represent the error weighted mean and standard error of the three individual spectra.

Table 2 presents our RV measurements. We found a mean RV of $7.51 \pm 0.23\,\mathrm{km\,s^{-1}}$, which is consistent with the value of $8.1 \pm 1.0\,\mathrm{km\,s^{-1}}$ found by Torres et al. (2006), but inconsistent with the more recent value of $-2.3 \pm 0.4\,\mathrm{km\,s^{-1}}$ reported by Chen et al. (2011). The discrepancy with the latter may be the result of the source's large rotational broadening (see Section 3.3), which results in Fourier cross-correlation functions that are not well fit by Gaussian profiles.

3.3. Projected Rotational Velocity

As a free parameter of the stellar line profile fit above, we also measure the projected rotational velocity $v \sin(i)$. From the mean and standard error for each data set, we measure a value of $54.9 \pm 0.1\,\mathrm{km\,s^{-1}}$ for the SALT:HRS spectra and $54.9 \pm 0.4\,\mathrm{km\,s^{-1}}$ from LCOGT:NRES. These fits do not include broadening contributions from microturbulence, but that is likely to have a small effect given the large $v \sin(i)$ measured. From the SMARTS:CHIRON observations we measure a value of $51.9 \pm 0.3\,\mathrm{km\,s^{-1}}$, and with FEROS we measure $v \sin(i)$ of $52.20 \pm 0.02\,\mathrm{km\,s^{-1}}$. These values are all consistent with the values reported by Torres et al. (2006; $51\,\mathrm{km\,s^{-1}}$) and Chen et al. (2011; $57 \pm 3\,\mathrm{km\,s^{-1}}$), and the variance between measurements likely reflects the treatment of broadening sources by the different analyses.

3.4. Stellar Rotation

The TESS light curve of HIP 67522 shows constant modulation of 1%–2% peak-to-peak amplitude on timescales shorter than 2 days. To determine the rotation period, we took the TESS light curve, masked out the transits of the candidate planets from the data, and computed a Lomb–Scargle periodogram spanning periods of 1–15 days. There are peaks in the periodogram at ∼0.71 and ∼1.4 days, the latter of which is consistent with period measurements from ground-based observations from Mellon et al. (2017). The light-curve morpohology in the second half of the TESS data set clearly indicates that the longer period is associated with the rotation of the star.

To determine the credible interval on the stellar rotation period, we fit the TESS light curve with a Gaussian process (GP) using the celerite package (Foreman-Mackey et al. 2017). We used a kernel composed of two stochastically driven, damped harmonic oscillators, with two Fourier modes: one at the rotation period of the star, and one at half the rotation period. This was done as part of our transit fitting methodology described in Section 5.1. We measure the rotation period to be 1.418 ± 0.016 days.

Given the measurements of the stellar rotation period, projected rotation velocity, and stellar radius, we can estimate both the equatorial velocity and hence the stellar inclination relative to our line of sight and the orbit of the transiting planet candidate. We compute an equatorial velocity for HIP 67522 of $49.2 \pm 2.2\,\mathrm{km\,s^{-1}}$ and use the Bayesian methodology of Morton & Winn (2014) to compute the likelihood of the stellar inclination. We find a loose constraint of $i > 66^{\circ}$ at 99% confidence, noting that we adopt $i < 90^{\circ}$ here, though we cannot distinguish between $i < 90^{\circ}$ and $i > 90^{\circ}$.

4. Membership in the Sco-Cen Association

HIP 67522 was first identified as a member of the Upper Centaurus-Lupus (UCL) subgroup of the Sco-Cen association on the basis of proper-motion comovement with other association members by de Zeeuw et al. (1999). HIP 67522 also features multiple spectral indicators of youth that support membership in Sco-Cen. In particular, HIP 67522 appears lithium rich for an early G dwarf and exhibits X-ray and Hα emission typical of other young stars in Sco-Cen (Mamajek et al. 2002; Chen et al. 2011).

We reassess the kinematic association of HIP 67522 with Sco-Cen on the basis of the new Gaia DR2 astrometry and photometry and our RV monitoring. The three-dimensional space motion of HIP 67522 is $(U, V, W) = (7.12, -21.53, -5.67) \pm (0.19, 0.22, 0.13)\,\mathrm{km\,s^{-1}}$. This is highly consistent with the velocity of UCL (Wright & Mamajek 2018). The distance of ∼127 pc also places HIP 67522 within 1σ of the Sco-Cen median distance ($d = 110 \pm 20$ pc) in that region of the association. We compute a membership probability for HIP 67522 in Sco-Cen of 96% following the Bayesian prescription of Rizzuto et al. (2011) and using the Gaia DR2 astrometry and the RV measured in Section 3.2. HIP 67522 is therefore a high-confidence kinematic member of the association.

The color–magnitude diagram (CMD) position of HIP 67522 places it in the association sequence. Figure 6 shows the Gaia ($R_P - G$, G) CMD for high-probability Sco-Cen members, as well as isochrones from the PARSEC 1.2 s models for ages of 15 and 20 Myr (Bressan et al. 2012).
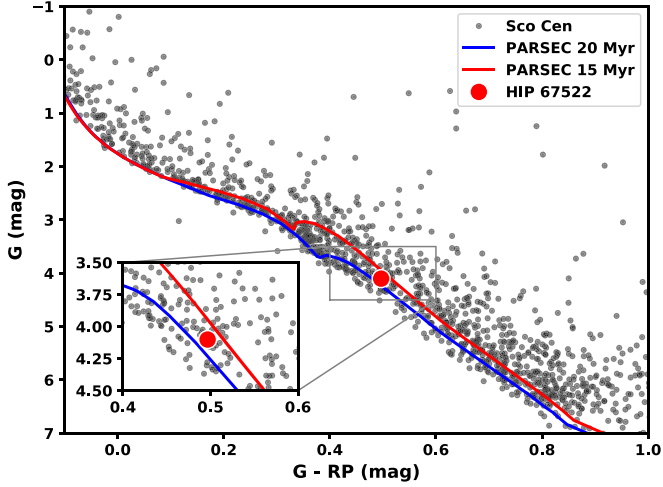
Figure 6. CMD for high-probability kinematic members of the Sco-Cen association, relative to HIP 67522 (red circle), produced using Gaia DR2 photometry and parallaxes (Lindegren et al. 2018). The red and blue lines are the PARSEC 1.2 s (Bressan et al. 2012) 15 and 20 Myr isochrones, respectively. HIP 67522 sits between the two isochrones, as expected for a member of UCL.

HIP 67522 falls between the isochrones of the two models, as is expected for UCL stars with ages ranging from 15 to 20 Myr.

5. Transit Fitting

5.1. HIP 67522 b

We fit a combined transit and variability model to the TESS and Spitzer photometry using the `misttborn` (Johnson et al. 2018) transit fitting code,[13] with the single transit candidate and any flares identified by inspection masked from the light curve. The transit model was generated with the BAsic Transit Model cAlculatioN (BATMAN; Kreidberg 2015) model to generate model light curves, and the stellar rotational variability was modeled with a GP using the `celerite` package (Foreman-Mackey et al. 2017). We chose a GP kernel that reasonably matched the rotational periodogram power spectrum, which is dominated by the rotation period and the first harmonic. Specifically, the kernel consisted of two stochastically driven, damped harmonic oscillators, one at the model rotation period and the second at the first harmonic (or half the rotation period), and a jitter term to account for the possibility of additional stochastic errors. The amplitude and oscillator quality factor of each component oscillator were allowed to vary, though the primary component was forced to be less damped than the first harmonic in all cases. We then used the `emcee` (Foreman-Mackey et al. 2013) affine-invariant MCMC package to explore the parameter space. The transit model described above consists of the following parameters: time of periastron (T_0); orbital period of the planet (P); planet-to-star radius ratio ($R_p/R_\star$); impact parameter (b); two eccentricity parameters $\sqrt{e}\sin\omega$ and $\sqrt{e}\cos\omega$, where e is the orbital eccentricity and ω is the argument of periastron; the stellar density ($\rho_\star/\rho_\odot$); the linear and quadratic limb-darkening coefficients for TESS ($q_{1,1}$, $q_{2,1}$) as per the triangular sampling prescription of Kipping (2013); and the corresponding limb-darkening coefficients for Spitzer ($q_{1,2}$, $q_{2,2}$). The GP parameters, all explored in log-space, were the variability amplitude of the fundamental oscillator ($\log A_1$), the quality factor


Table 3
Properties of the Host Star HIP 67522 (TIC 166527623)

Parameter	Value	Source
Astrometry		
R.A.	13 50 06.280	TIC
Decl.	−40 50 08.88	TIC
μ_α (mas yr^{-1})	−28.843 ± 0.108	Gaia DR2
μ_δ (mas yr^{-1})	−22.425 ± 0.107	Gaia DR2
π (mas)	7.8288 ± 0.0671	Gaia DR2
Photometry		
G_{Gaia} (mag)	9.6326 ± 0.0023	Gaia DR2
BP_{Gaia} (mag)	9.9859 ± 0.0038	Gaia DR2
RP_{Gaia} (mag)	9.1359 ± 0.0038	Gaia DR2
B (mag)	10.571 ± 0.014	APASS
B_T (mag)	10.591 ± 0.036	TYCHO 2
V_T (mag)	9.876 ± 0.026	TYCHO 2
g' (mag)	10.830 ± 0.030	APASS
J (mag)	8.587 ± 0.021	2MASS
H (mag)	8.287 ± 0.042	2MASS
Ks (mag)	8.164 ± 0.026	2MASS
$W1$ (mag)	8.108 ± 0.022	ALLWISE
$W2$ (mag)	8.122 ± 0.019	ALLWISE
$W3$ (mag)	8.077 ± 0.018	ALLWISE
$W4$ (mag)	8.121 ± 0.186	ALLWISE
Kinematics and Position		
Barycentric RV (km s^{-1})	7.41 ± 0.25	This paper
U (km s^{-1})	7.12 ± 0.19	This paper
V (km s^{-1})	−21.53 ± 0.22	This paper
W (km s^{-1})	−5.67 ± 0.13	This paper
X (pc)	−84.15 ± 0.73	This paper
Y (pc)	−84.89 ± 0.74	This paper
Z (pc)	45.13 ± 0.39	This paper
Distance (pc)	$127.27^{+1.10}_{-1.08}$	Bailer-Jones et al. (2018)
Physical Properties		
Rotation period (days)	1.418 ± 0.016	This paper
$v\sin i$ (km s^{-1})	54.2 ± 0.7	This paper
F_{bol}(erg cm^{-2} s^{-1})	(3.44 ± 0.17) × 10^{-9}	This paper
T_{eff} (K)	5675 ± 75	This paper
$M_\star (M_\odot)$	1.22 ± 0.05	This paper
$R_\star (R_\odot)$	1.38 ± 0.06	This paper
$L_\star (L_\odot)$	1.75 ± 0.09	This paper
$\rho_\star (\rho_\odot)$	0.46 ± 0.06	This paper
Age (Myr)	17 ± 2	This paper
$E(B-V)$ (mag)	0.04 ± 0.02	This paper

of the half-period oscillator ($\log Q_2$), the difference in quality factors for the two oscillators ($\Delta Q = Q_1 - Q_2$), the rotation period ($\log P_R$), and a mixture term describing the amplitude ratio of the two oscillators (m, where $A_1/A_2 = 1 + e^{-m}$). The mixture term, m, was formulated in this way to facilitate sampling without the requirement for bounds while ensuring that the oscillator at the full rotation period had the largest amplitude. Finally, the stochastic jitter term had a single parameter ($\log \sigma_j^2$) that represented the variance of the jitter model.

We applied Gaussian priors on the limb-darkening coefficients for both TESS and Spitzer based on the values in Claret & Bloemen (2011) and Claret (2017). We also used Gaussian priors for the stellar density, taken from our derived stellar parameters in Table 3. All other parameters were sampled uniformly, with

---
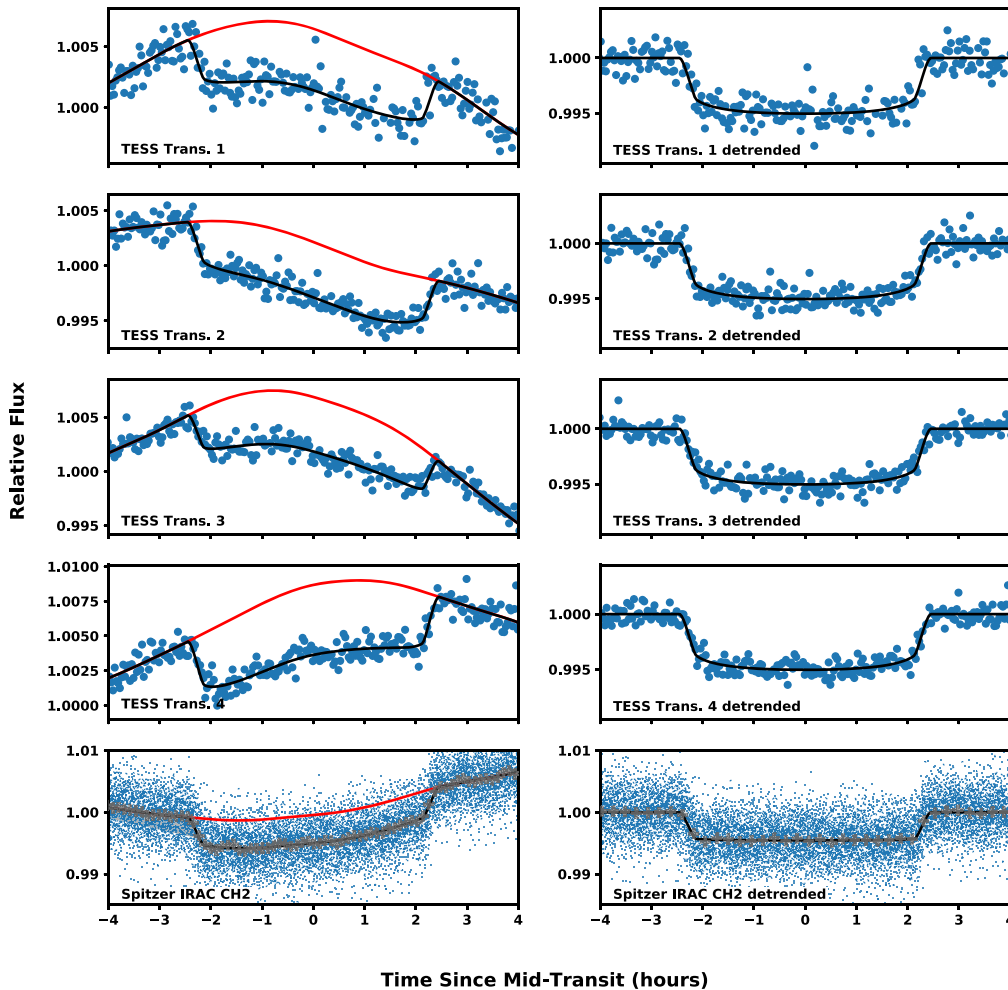
Figure 7. Five transits of HIP 67522 b, four from TESS and one from Spitzer IRAC channel 2 (corrected using BLISS), with and without GP detrending. Left column: transits without variability removed using the GP model. Blue points are the photometry, the black line is the full transit and GP model, and the red line is the GP model only. Right column: same data with the GP model component removed. The black line now shows the best-fit transit model. In the two plots containing Spitzer data, the gray plus signs are the data binned into 70 bins.

physically motivated boundaries, namely, $\sqrt{e}\sin\omega$ and $\sqrt{e}\cos\omega$ bound by $(-1, 1)$, and $|b| < 1 + R_p/R_s$. The GP parameters were allowed to vary without bounds on the real line, except for ΔQ, which was set to be larger than zero. We used 50 walkers in the MCMC, running 240,000 steps each, with a burn-in of 120,000 steps. These chain lengths correspond to 100 and 60 times the integrated autocorreltaion times, respectively, described in Goodman & Weare (2010). The resulting fit is shown in Figure 1, with the individual transits shown in Figure 7, and the best-fitting model and derived parameters, along with 68% credible intervals, are listed in Table 4. Figures 8 and 9 show the posteriors for the transit fit parameters.

5.1.1. False Positive Probability

Given the $\sim 2''$ resolution of the Spitzer imaging, it is possible that the transit signals of HIP 67522 b are caused by some astrophysical system other than a transiting exoplanet. We directly address some of these false positive scenarios for HIP 67522 b as follows:

1. *The transits are caused by instrumental artifacts or residuals from stellar variability*: though the four transits of HIP 67522b in the TESS data set have amplitudes much smaller than the amplitude of starspot variability, we confirm the transits with Spitzer, conclusively.

2. *HIP 67522 is an eclipsing binary or brown dwarf*: We generated 1,000,000 binary companions with a uniform distribution in all orbital parameters except a Gaussian distribution in period following Raghavan et al. (2010) and the inclination restricted to values where the companion would eclipse the primary ($i \simeq 90°$). We then compared the predicted RVs to those we measured from our high-resolution spectroscopy (Section 3.2), rejecting systems that disagree with the data at $>3\sigma$. For this comparison, we added in a conservative $150\,\mathrm{m\,s^{-1}}$ jitter (in quadrature) to all points to account for the star's activity levels. All companions with nonplanetary masses and periods below 80 days can be ruled out. We set a 2σ limit on the mass of the planet of $M_p < 5M_J$.

3. *The transits are blended from a background, unassociated eclipsing binary system or transiting exoplanet*: We take the same approach outlined in Vanderburg et al. (2019). In short, if the transits are a blend from the background system, the true radius ratio is constrained by the ratio of the ingress time (T_{12}) to the duration from first to third contact (T_{13}), and we can estimate the largest

Table 4
Transit Fit Parameters for HIP 67522b

Parameter	TESS Only	TESS + IRAC CH2
Fit Parameters		
T_0 (BJD)	$2458604.02358^{+0.00041}_{-0.00041}$	$2458604.02371^{+0.00036}_{-0.00037}$
P (days)	$6.95993^{+0.00034}_{-0.00034}$	$6.959503^{+0.000016}_{-0.000015}$
$R_P/R_\star$	$0.0645^{+0.0015}_{-0.0015}$	$0.0667^{+0.0012}_{-0.0011}$
b	$0.15^{+0.13}_{-0.1}$	$0.134^{+0.106}_{-0.092}$
$\rho_\star(\rho_\odot)$	$0.455^{+0.052}_{-0.049}$	$0.448^{+0.055}_{-0.049}$
$\sqrt{e}\sin\omega$	$-0.055^{+0.103}_{-0.084}$	$-0.053^{+0.106}_{-0.084}$
$\sqrt{e}\cos\omega$	$0.00^{+0.34}_{-0.34}$	$0.00^{+0.34}_{-0.35}$
$q_{1,1}$	$0.157^{+0.099}_{-0.073}$	$0.241^{+0.087}_{-0.068}$
$q_{1,2}$	$0.20^{+0.16}_{-0.13}$	$0.22^{+0.15}_{-0.13}$
$q_{1,2}$	...	$0.014^{+0.024}_{-0.010}$
$q_{2,2}$	...	$0.160^{+0.101}_{-0.089}$
GP Parameters		
$\log A_1$	$-10.45^{+0.47}_{-0.28}$	$-10.44^{+0.37}_{-0.26}$
$\log Q_1$	$4.68^{+0.79}_{-0.74}$	$4.59^{+0.75}_{-0.72}$
A_2/A_1	$0.9916^{+0.0081}_{-0.2544}$	$0.9905^{+0.0092}_{-0.2068}$
$\log Q_2$	$2.02^{+0.32}_{-0.25}$	$2.00^{+0.28}_{-0.24}$
$P_{\rm Rot}$ (days)	$1.422^{+0.014}_{-0.016}$	$1.422^{+0.014}_{-0.016}$
$\log\sigma$	$-15.7^{+3.1}_{-2.9}$	$-15.3^{+2.9}_{-3.1}$
Derived Parameters		
$a/R_\star$	$11.73^{+0.24}_{-0.28}$	$11.70^{+0.24}_{-0.27}$
i (deg)	$89.27^{+0.51}_{-0.67}$	$89.34^{+0.45}_{-0.54}$
T_{14} (hr)	$4.786^{+0.032}_{-0.030}$	$4.822^{+0.021}_{-0.019}$
R_P ($R_\oplus$)	$9.72^{+0.48}_{-0.47}$	$10.07^{+0.47}_{-0.47}$
e	$0.061^{+0.172}_{-0.047}$	$0.059^{+0.193}_{-0.046}$
ω (deg)	-21^{+86}_{-145}	-17^{+92}_{-149}
$T_{\rm eq}(K)$	1173^{+21}_{-20}	1174^{+21}_{-20}
$u_{1,1}$	$0.148^{+0.111}_{-0.093}$	$0.22^{+0.12}_{-0.12}$
$u_{1,2}$	$0.23^{+0.16}_{-0.14}$	$0.27^{+0.15}_{-0.15}$
$u_{1,2}$	...	$0.033^{+0.037}_{-0.021}$
$u_{2,2}$	…	$0.076^{+0.061}_{-0.043}$

Note.
a Equilibrium temperature $T_{\rm eq}$ was calculated assuming zero albedo.

possible magnitude difference between HIP 67522 and a background object that could produce the transits as $\Delta m \leqslant 2.5\log_{10}(t_{12}^2/t_{13}^2/\delta)$, where δ is the observed transit depth. We repeat the transit fitting described in Section 5.1 with the prior on stellar density and limb darkening removed to explore the allowed posterior for the duration terms. This yields $\Delta m < 2.6$ mag at 99.9% confidence. Interpolating on the Baraffe et al. (2015) 2 Gyr isochrone, this is equivalent to a companion of mass $>0.74\,M_\odot$. The imaging and astrometric limits to companions presented in Table 5 rule out such objects down to $\sim$60 mas.

4. *HIP 67522 is a hierarchical triple*: We generate an additional 1,000,000 companions as above, but now assign orbital periods based on a lognormal distribution following Raghavan et al. (2010). We compare each binary to the AO, RV, and Gaia-derived constraints on companions, adding jitter to the velocity data as in the first scenario. We exclude companions too faint to reproduce the observed transit depth (following the method above) and those that would be

resolved in the Spitzer imaging. Because bound companions would be younger and brighter than a typical field star, the constraints are stronger than the background eclipsing binary case; less than 1% of the generated companions survive. Survivors that could have reproduced the transit depth are generally companions that happen to be aligned with the host star in the plane of the sky. Considering that the underlying rate of hierarchical triples is $\simeq$16% Raghavan et al. (2010), this scenario is ruled out statistically. We do not include constraints from chromaticity of the transit depths (TESS vs. Spitzer), which would strengthen the constraints (Désert et al. 2015).

We quantify the likelihood of one of the above scenarios causing the transits of HIP 67522 b using the open-source vespa software package (Morton 2015). Vespa computes the false positive probability (FPP) according to Morton (2012) and Morton et al. (2016). This is done with a Bayesian model comparison between various scenarios that may cause transit-like signals (such as an exoplanet, background eclipsing binaries, eclipsing binary on the primary, and eclipsing binary on a companion) using the transit photometry, observational constraints on companions, and the host star parameters and photometry. We ran vespa with the stellar parameters of HIP 67522 in Table 3, the TESS light curve with the GP model described in Section 5 subtracted, and the constraints to companions from the speckle imaging and Gaia astrometry from Table 5. Based on these inputs, vespa calculated an FPP $< 1 \times 10^{-6}$ for HIP 67522 b. We hence consider HIP 67522 b to be a validated exoplanet.

5.2. Single Transit Parameters

We model the single transit with the same methodology as was used for the periodic signal in Section 5.1, with modification to allow for an unconstrained orbital period. We use the same GP to model the out-of-transit rotation variability but constrain the parameters with Gaussian priors with standard deviation equal to the 68% credible intervals from the periodic fit shown in Table 4. Similarly, we constrain the limb-darkening parameters in the TESS bandpass, q_1 and q_2, and the stellar density $\rho_\star/\rho_\odot$ based on the previous fit. We allowed the orbital parameters to vary as in Section 5.1 and applied an unbiased prior on eccentricity taken from Kipping (2014).

Beyond the transit shape, we also have some information regarding the orbital period of the candidate exoplanet based on the lack of an additional transit in the TESS Sector 11 data set. Similarly to Vanderburg et al. (2018), we apply this as a prior in the MCMC to the estimated periods based on the time baseline of the TESS light curve for HIP 67522:

$$P(P_{\rm single}) \propto (\tau + T_{14})/P_{\rm single}, \qquad (1)$$

where τ is the time baseline of the TESS observation in sector 11 (23 days) and T_{14} is the duration of the transit including ingress and egress. We explored our model posterior using an MCMC framework and the emcee package (Foreman-Mackey et al. 2013). We used 40 walkers and iterated for 200,000 steps with a 100,000-step burn-in. Figure 10 shows the single transit and best-fit model, and Table 6 lists the best-fit model parameters.
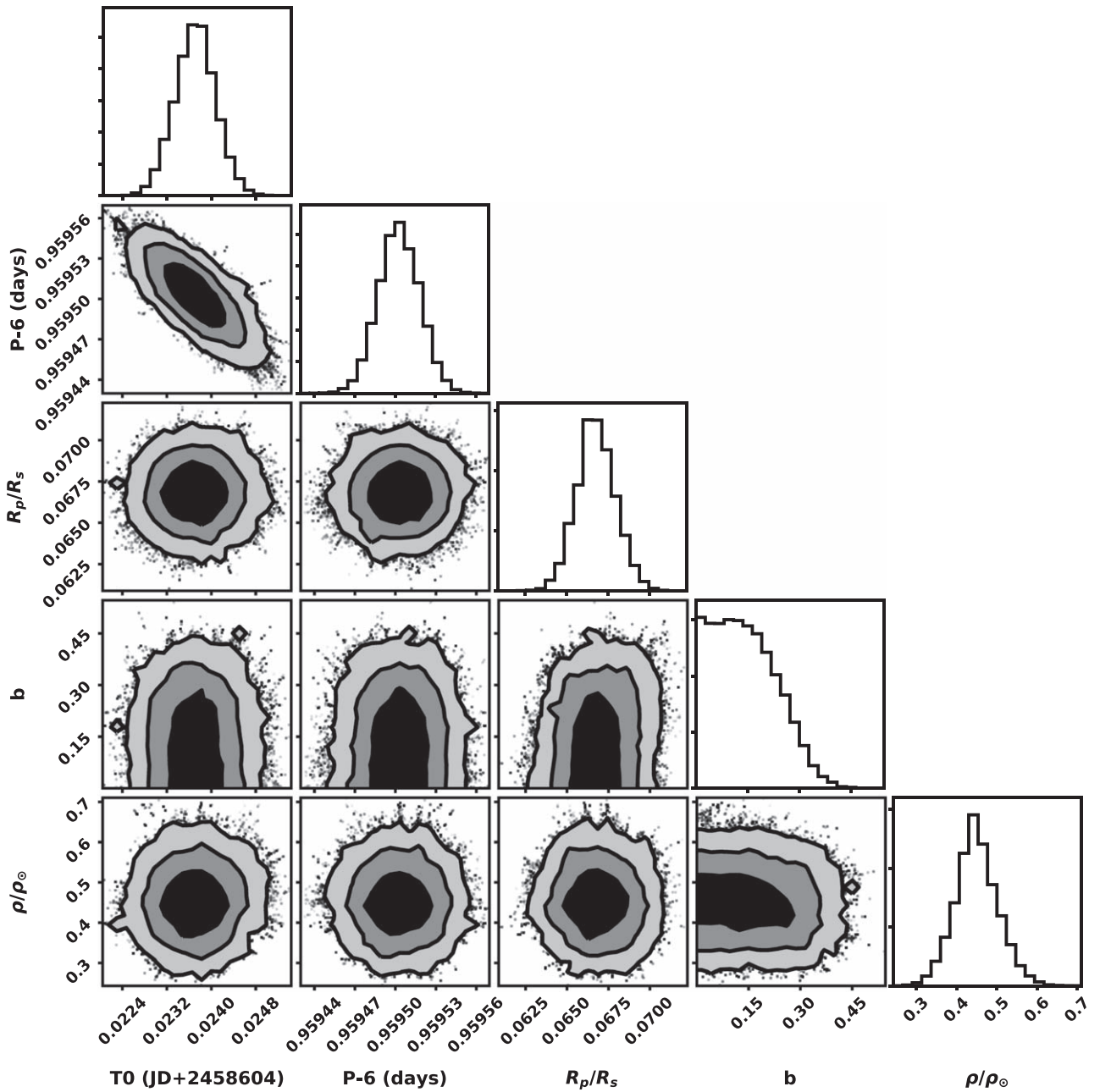
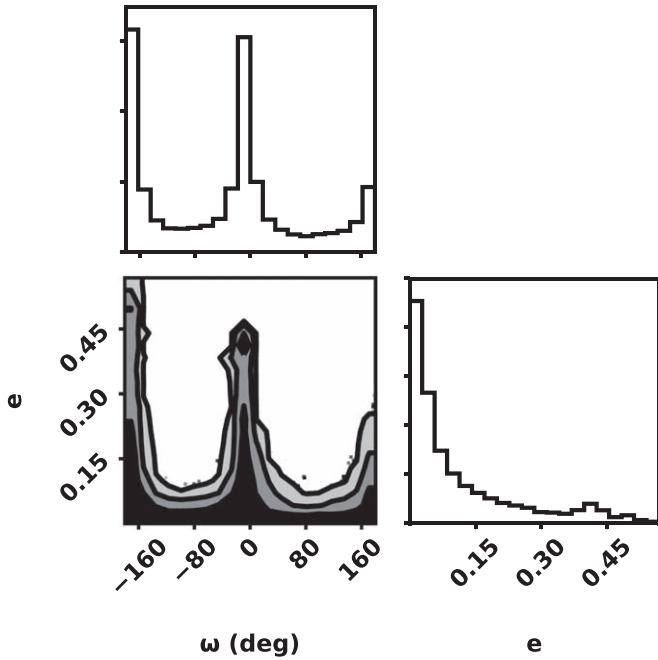**Figure 8.** Selected transit fit posteriors for HIP 67522b.

6. Discussion

We have reported the detection and characterization of a 17 Myr old transiting giant planet, HIP 67522b in the Sco-Cen association, with an orbital period of 6.9596 days and a candidate second planet in a much longer period orbit. HIP 67522b is currently the youngest confirmed transiting, hot, Jupiter-sized planet, pending the confirmation of the possible hot Jupiter PTFO 8–8695b (CVSO-30 b; van Eyken et al. 2012; Yu et al. 2015; Johns-Krull et al. 2016). HIP 67522 b is one of only a small handful of exoplanets younger than 20 Myr (K2–33 b, Mann et al. 2016b; V1298 Tau bcde, David et al. 2019) and as such may be significant as a benchmark young system in future models of exoplanet formation and migration.

HIP 67522 b has a radius measured from the transit data from TESS and Spitzer of $R_P = 10.02^{+0.54}_{-0.53} R_\oplus$. The exoplanet

mass–radius relationship of Chen & Kipping (2017) and the constraints to planet masses given in Section 5.1.1 predict a mass in the range of 0.18–7.2 M_J. Our RV monitoring in Section 3.2 indicates a mass $M_P < 5 M_J$, ruling out the highest part of this range. Given the youth of the system, a mass–radius relation drawn from mature exoplanet systems with ages <1 Gyr may not directly apply. In particular, the radius of HIP 67522 b may be inflated for its true mass, as has been suggested for members of open clusters with ages <1 Gyr (e.g., Mann et al. 2017; Rizzuto et al. 2018).

The transits of HIP 67522 b are unlikely to be caused by a nonplanetary phenomenon; we calculate an FPP using vespa of 1×10^{-6}. From a combination of speckle imaging and analysis of the astrometric data from the Gaia DR2 catalog, we find no evidence for stellar or brown dwarf companions down to ∼100 mas. High-resolution spectroscopic monitoring of

Figure 9. Transit fit posteriors for eccentricity and argument of periastron (ω).

Table 5
Combined Contrast Limits for Companions to HIP 67522 from SOAR Speckle Imaging and Gaia Astrometry

			SOAR Speckle				
ρ (arcsec)	0.05	0.1	0.2	0.25	1.0	3.1	
ρ (au)	6.4	13	26	32	128	396	
ΔI^a (mag)	1.0	2.2	2.7	4.8	5.9	7.5	
Mass ($M_\odot$)	1.0	0.66	0.51	0.16	0.08	0.03	
			Gaia DR2 Astrometry				
ρ (arcsec)	0.03	0.08	0.20	2	3	6	>7
ρ (au)	4	10	25	255	383	766	>900
ΔG (mag)	0	4	5	6	8	10	11.0
Mass ($M_\odot$)	1.2.	0.5	0.3.	0.17	0.06	0.02	0.015

Note. Corresponding mass limits are taken from the BHAC15 isochrone of 17 Myr age (Baraffe et al. 2015).

HIP 67522 rules out spectroscopic companions with masses larger than 13 M_J.

We also detect a single transit of a third body in the HIP 67522 system in the TESS light curve, which we will tentatively refer to as HIP 67522 c. From fitting transit models to the single transit of HIP 67522 c, we find a radius of $8.01^{+0.75}_{-0.71}$ $R_\oplus$ and an orbital period that must be larger than ~24 days. The upcoming TESS first extended mission (Huang et al. 2018), which will revisit much of the Sco-Cen association, may provide confirmation of HIP 67522 c in Sector 38 if the true orbital period is not significantly longer than the typical TESS observing sector length. We calculate the probability of TESS observing a transit if HIP 67522 c is in Sector 38 based on the period posterior from our transit model in Section 5.2 to be ~54%.

The constraints from the stellar parameters of HIP 67522 and the duration of the transits in the TESS and Spitzer light curves imply zero eccentricity for the orbit of HIP 67522 b (Figure 9).
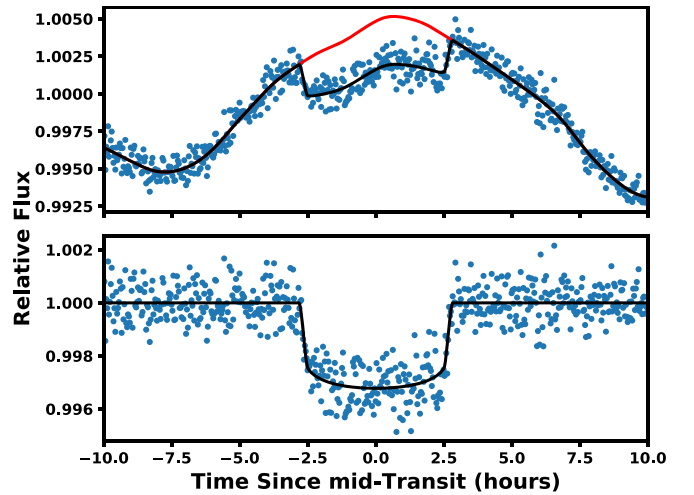
Figure 10. Transit of the singly transiting object and best-fit model. The top panel shows the presearch data conditioning (PDC) light curve (blue circles) with the GP model (red) and GP with transit model (black), while the bottom panel shows the same with the GP model removed.

Table 6
Transit Fit Parameters for HIP 67522c

Parameter	
T_0 (BJD)	2458602.5026 ± 0.0014
P (days)	$54^{+70}_{-24.0}$
$R_P/R_\star$	$0.0532^{+0.0044}_{-0.0041}$
b	$0.52^{+0.23}_{-0.33}$
e	$0.29^{+0.15}_{-0.14}$
ω^a (deg)	$74^{+56}_{-53.0}$
$R_P{}^a$ ($R_\oplus$)	$8.01^{+0.75}_{-0.71}$
$T_{14}{}^a$ (hr)	$5.707^{+0.127}_{-0.09}$
i^A (deg)	$89.56^{+0.29}_{-0.42}$
$a/R_\star{}^a$	$56^{+58}_{-21.0}$
$T_{eq}{}^b$ (K)	573^{+113}_{-163}

Notes.
[a] R_P, ω, e, full transit duration T_{14}, inclination i, and semimajor axis $a/R_\star$ were not directly fit but derived from the fit parameters and stellar parameters from Table 3.
[b] Equilibrium temperature T_{eq} was calculated assuming zero albedo.

Large eccentricities (>0.3) are strongly ruled out (Figure 9). The stellar rotation axis is also weakly constrained to be aligned to the orbital plane. In combination with the presence of the outer planet HIP 67522 c, this suggests possible formation or migration mechanisms responsible for the architecture of this system. In particular, the existence of a short-period hot Jupiter at 17 Myr itself means that it is possible to produce a short-period gas giant while still on the early pre–main sequence. Disk migration can induce migration to short periods on such timescales (Lubow & Ida 2010), and disk–planet interactions are not expected to produce eccentricities larger than $e \sim 0.05$–0.1 (Dunhill et al. 2013). Indeed, disk migration is expected to produce gas giants in short-period orbits (<20 days) on timescales shorter than the age of HIP 67522 with close-to-zero eccentricities (Cloutier & Lin 2013). This scenario is consistent with the transit parameters we have measured for HIP 67522 b.

The presence of a second planet on a transiting orbit with period <100 days, as is likely for HIP 67522 c pending confirmation, is

somewhat rare for a hot Jupiter system (Wright et al. 2009; Szabó et al. 2013), though some examples exist (e.g., Vanderburg et al. 2017). This architecture may suggest either ongoing dynamical interactions or that HIP 67522 b is in fact less massive than its radius implies. Dynamical interactions between planets, such as planet–planet scattering (Chatterjee et al. 2008), and the Kozai–Lidov interaction (Fabrycky & Tremaine 2007) are expected to produce eccentric and often misaligned warm/hot Jupiters. The timescales involved for these interactions are typically 100–1000 Myr, longer than the ∼17 Myr age of HIP 67522. Given the presence of HIP 67522 c, planet–planet interactions may be important in this system, and orbital evolution of the HIP 67522 b-c system may still be ongoing.

6.1. Prospects for Follow-up

The relative brightness ($V = 9.8$ mag) and proximity ($d = 127$ pc) of HIP 67522 make it highly amenable to follow-up, with both ground-based and space-based observatories. Measuring the mass of HIP 67522 b would provide a rare young-age density measurement and would allow comparison to older counterparts. Given the mass estimate from Chen & Kipping (2017) of $M = 0.18$–$4.6\,M_J$, the expected RV amplitude will be in the range of 17–400 ms^{-1}. At the upper end, this is comparable to the expected RV variability due to rotation of 150 m s^{-1}, calculated using $\Delta \mathrm{RV} = \sigma_{\mathrm{phot}} v \sin i$, where σ_{phot} is the photometric variability amplitude in the same band. It will certainly be possible to either detect or rule out the most massive scenarios for HIP 67522 b with future RV measurements. A dedicated campaign designed to observe and model the RV systematics, perhaps in the near-IR, where variability is expected to be smaller, may allow a mass measurement even for the smaller side of the possible mass values (e.g., Barragán et al. 2019).

A measurement of the sky-projected angle between the orbital rotation and stellar rotation angular momentum vectors via observation of the Rossiter–McLaughlin (RM) effect for HIP 67522 b is also possible. We estimate the size of the RV amplitude due to the Rossiter–McLoughlin effect to be ∼160 ms^{-1} using the relation $\Delta \mathrm{RV}_{\mathrm{RM}} = 0.65 v \sin i (R_p/R_\star)^2 \sqrt{1 - b^2}$ (Gaudi & Winn 2007), making this one of the most amenable targets for RM follow-up. Constraining the star–planet obliquity of this young system may shed light on potential migration of dynamical evolution processes responsible for its production (e.g., Montet et al. 2020; Zhou et al. 2020).

HIP 67522 b is also a strong candidate for atmospheric characterization with the James Webb Space Telescope (JWST). We compute the transmission spectroscopy metric as described in Kempton et al. (2018) to be ∼190, assuming zero albedo and full day-night heat redistribution to derive an equilibrium temperature of $T_{\mathrm{eq}} = 1174 \pm 21$ K and a mass of $0.25\,M_J$ as per the prescription of Kempton et al. (2018) and Chen & Kipping (2017). This can be interpreted as a transmission spectrum measurement with a signal-to-noise ratio of ∼190 in a 10 hr window with the NIRISS instrument (Louie et al. 2018). This places HIP 67522 b in the top quartile of transiting gas giants for JWST atmospheric characterization. Combined with its young age, this makes HIP 67522 a compelling target for further characterization.

Facilities: TESS, SALT (HRS), SOAR (Goodman), WASP, Spitzer, light curve (NRES), CDS, MAST, SIMBAD.
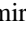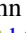
Software: Astropy (Astropy Collaboration et al. 2013, 2018), emcee (Foreman-Mackey et al. 2013), celerite (Foreman-Mackey et al. 2017) VESPA (Morton 2015), SPOC pipeline (Jenkins 2015; Jenkins et al. 2016), misttborb (Johnson et al. 2018), BATMAN (Kreidberg 2015), POET (Campo et al. 2011; Stevenson et al. 2012).

---

[14] http://www.tacc.utexas.edu
[15] https://www.cosmos.esa.int/gaia
[16] https://www.cosmos.esa.int/web/gaia/dpac/consortium

ORCID iDs

Aaron C. Rizzuto ⓘ https://orcid.org/0000-0001-9982-1332
Elisabeth R. Newton ⓘ https://orcid.org/0000-0003-4150-841X
Andrew W. Mann ⓘ https://orcid.org/0000-0003-3654-1602
Benjamin M. Tofflemire ⓘ https://orcid.org/0000-0003-2053-0749
Andrew Vanderburg ⓘ https://orcid.org/0000-0001-7246-5438
Adam L. Kraus ⓘ https://orcid.org/0000-0001-9811-568X
Mackenna L. Wood ⓘ https://orcid.org/0000-0001-7336-7725
Samuel N. Quinn ⓘ https://orcid.org/0000-0002-8964-8377
George Zhou ⓘ https://orcid.org/0000-0002-4891-3517
Pa Chia Thao ⓘ https://orcid.org/0000-0001-5729-6576
Nicholas M. Law ⓘ https://orcid.org/0000-0001-9380-6457
Carl Ziegler ⓘ https://orcid.org/0000-0002-0619-7639
César Briceño ⓘ https://orcid.org/0000-0001-7124-4094

References

Adams, F. C., & Laughlin, G. 2006, ApJ, 649, 1004
Allard, F., Homeier, D., & Freytag, B. 2011, in ASP Conf. Ser. 448, 16th Cambridge Workshop on Cool Stars, Stellar Systems, and the Sun, ed. C. Johns-Krull, M. K. Browning, & A. A. West (San Francisco, CA: ASP), 91
Astropy Collaboration, Price-Whelan, A. M., Sipőcz, B. M., et al. 2018, AJ, 156, 123
Astropy Collaboration, Robitaille, T. P., Tollerud, E. J., et al. 2013, A&A, 558, A33
Bailer-Jones, C. A. L., Rybizki, J., Fouesneau, M., Mantelet, G., & Andrae, R. 2018, AJ, 156, 58
Baraffe, I., Homeier, D., Allard, F., & Chabrier, G. 2015, A&A, 577, A42
Barragán, O., Aigrain, S., Kubyshkina, D., et al. 2019, MNRAS, 490, 698
Bessell, M., & Murphy, S. 2012, PASP, 124, 140
Bowler, B. P. 2016, PASP, 128, 102001
Brandeker, A., & Cataldi, G. 2019, A&A, 621, A86
Bressan, A., Marigo, P., Girardi, L., et al. 2012, MNRAS, 427, 127
Buckley, D. A. H., Swart, G. P., & Meiring, J. G. 2006, Proc. SPIE, 6267, 62670Z
Cai, M. X., Kouwenhoven, M. B. N., Portegies Zwart, S. F., & Spurzem, R. 2017, MNRAS, 470, 4337
Campo, C. J., Harrington, J., Hardy, R. A., et al. 2011, ApJ, 727, 125
Castelli, F., & Kurucz, R. L. 2004, arXiv:astro-ph/0405087
Chatterjee, S., Ford, E. B., Matsumura, S., & Rasio, F. A. 2008, ApJ, 686, 580
Chen, C. H., Mamajek, E. E., Bitner, M. A., et al. 2011, ApJ, 738, 122
Chen, J., & Kipping, D. 2017, ApJ, 834, 17
Claret, A. 2017, A&A, 600, A30
Claret, A., & Bloemen, S. 2011, A&A, 529, A75
Clemens, J. C., Crain, J. A., & Anderson, R. 2004, Proc. SPIE, 5492, 331
Cloutier, R., & Lin, M.-K. 2013, MNRAS, 434, 621
Cohen, M., Wheaton, W. A., & Megeath, S. T. 2003, AJ, 126, 1090
Crause, L. A., Sharples, R. M., Bramall, D. G., et al. 2014, Proc. SPIE, 9147, 91476T
David, T. J., Cody, A. M., Hedges, C. L., et al. 2019, AJ, 158, 79
David, T. J., Hillenbrand, L. A., Petigura, E. A., et al. 2016, Natur, 534, 658
de Zeeuw, P. T., Hoogerwerf, R., de Bruijne, J. H. J., Brown, A. G. A., & Blaauw, A. 1999, AJ, 117, 354
Désert, J.-M., Charbonneau, D., Torres, G., et al. 2015, ApJ, 804, 59
Dunhill, A. C., Alexander, R. D., & Armitage, P. J. 2013, MNRAS, 428, 3072
Ehrenreich, D., Bourrier, V., Wheatley, P. J., et al. 2015, Natur, 522, 459
Fabrycky, D., & Tremaine, S. 2007, ApJ, 669, 1298
Fazio, G. G., Hora, J. L., Allen, L. E., et al. 2004, ApJS, 154, 10
Foreman-Mackey, D., Agol, E., Ambikasaran, S., & Angus, R. 2017, AJ, 154, 220
Foreman-Mackey, D., Hogg, D. W., Lang, D., & Goodman, J. 2013, PASP, 125, 306
Gaudi, B. S., & Winn, J. N. 2007, ApJ, 655, 550
Goodman, J., & Weare, J. 2010, CAMCS, 5, 65
Gupta, A., & Schlichting, H. E. 2019, MNRAS, 487, 24
Henden, A. A., Levine, S. E., Terrell, D., Smith, T. C., & Welch, D. 2012, JAVSO, 40, 430
Hippke, M., & Heller, R. 2019, A&A, 623, A39
Howell, S. B., Sobeck, C., Haas, M., et al. 2014, PASP, 126, 398
Huang, C. X., Shporer, A., Dragomir, D., et al. 2018, arXiv:1807.11129
Husser, T.-O., Wende-von Berg, S., Dreizler, S., et al. 2013, A&A, 553, A6
Ingalls, J. G., Krick, J. E., Carey, S. J., et al. 2012, Proc. SPIE, 8442, 84421Y
Ingalls, J. G., Krick, J. E., Carey, S. J., et al. 2016, AJ, 152, 44
James, D. J., Melo, C., Santos, N. C., & Bouvier, J. 2006, A&A, 446, 971
Jenkins, J. M. 2015, AAS/ESS Meeting, 47, 106.05
Jenkins, J. M., Twicken, J. D., McCauliff, S., et al. 2016, Proc. SPIE, 9913, 99133E
Johns-Krull, C. M., Prato, L., McLane, J. N., et al. 2016, ApJ, 830, 15
Johnson, M. C., Dai, F., Justesen, A. B., et al. 2018, MNRAS, 481, 596
Kaufer, A., Stahl, O., Tubbesing, S., et al. 1999, Msngr, 95, 8
Kempton, E. M.-R., Bean, J. L., Louie, D. R., et al. 2018, PASP, 130, 114401
Kipping, D. M. 2013, MNRAS, 435, 2152
Kipping, D. M. 2014, MNRAS, 444, 2263
Kniazev, A. Y., Gvaramadze, V. V., & Berdnikov, L. N. 2016, MNRAS, 459, 3068
Kovács, G., Zucker, S., & Mazeh, T. 2002, A&A, 391, 369
Kraus, A. L., & Hillenbrand, L. A. 2008, ApJL, 686, L111
Kreidberg, L. 2015, PASP, 127, 1161
Lindegren, L., Hernández, J., Bombrun, A., et al. 2018, A&A, 616, A2
Lopez, E. D., Fortney, J. J., & Miller, N. 2012, ApJ, 761, 59
Louie, D. R., Deming, D., Albert, L., et al. 2018, PASP, 130, 044401
Lubow, S. H., & Ida, S. 2010, arXiv:1004.4137
Mainzer, A., Bauer, J., Grav, T., et al. 2011, ApJ, 731, 53
Maíz Apellániz, J., & Weiler, M. 2018, A&A, 619, A180
Mamajek, E. E., Meyer, M. R., & Liebert, J. 2002, AJ, 124, 1670
Mann, A. W., Feiden, G. A., Gaidos, E., Boyajian, T., & von Braun, K. 2015, ApJ, 804, 64
Mann, A. W., Gaidos, E., & Gaudi, B. S. 2010, ApJ, 719, 1454
Mann, A. W., Gaidos, E., Mace, G. N., et al. 2016a, ApJ, 818, 46
Mann, A. W., Gaidos, E., Vanderburg, A., et al. 2017, AJ, 153, 64
Mann, A. W., Newton, E. R., Rizzuto, A. C., et al. 2016b, AJ, 152, 61
Mann, A. W., & von Braun, K. 2015, PASP, 127, 102
Mellon, S. N., Mamajek, E. E., Oberst, T. E., & Pecaut, M. J. 2017, ApJ, 844, 66
Montet, B. T., Feinstein, A. D., Luger, R., et al. 2020, AJ, 159, 112
Morton, T. D. 2012, ApJ, 761, 6
Morton, T. D. 2015, VESPA: False Positive Probabilities Calculator, version 0.6, Astrophysics Source Code Library, ascl:1503.011
Morton, T. D., Bryson, S. T., Coughlin, J. L., et al. 2016, ApJ, 822, 86
Morton, T. D., & Winn, J. N. 2014, ApJ, 796, 47
Nielsen, E. L., de Rosa, R. J., Macintosh, B., et al. 2019, AJ, 158, 13
Pecaut, M. J., & Mamajek, E. E. 2016, MNRAS, 461, 794
Pecaut, M. J., Mamajek, E. E., & Bubar, E. J. 2012, ApJ, 746, 154
Perryman, M. A. C., & ESA (ed.) 1997, in ESA Special Pub. 1200, The HIPPARCOS and TYCHO catalogues. Astrometric and Photometric Star Catalogues Derived from the ESA HIPPARCOS Space Astrometry Mission (Noordwijk: ESA)
Quinn, S. N., White, R. J., Latham, D. W., et al. 2014, ApJ, 787, 27
Raghavan, D., McAlister, H. A., Henry, T. J., et al. 2010, ApJS, 190, 1
Ricker, G. R., Winn, J. N., Vanderspek, R., et al. 2014, Proc. SPIE, 9143, 914320
Rizzuto, A. C., Ireland, M. J., & Kraus, A. L. 2015, MNRAS, 448, 2737
Rizzuto, A. C., Ireland, M. J., & Robertson, J. G. 2011, MNRAS, 416, 3108
Rizzuto, A. C., Mann, A. W., Vanderburg, A., Kraus, A. L., & Covey, K. R. 2017, AJ, 154, 224
Rizzuto, A. C., Vanderburg, A., Mann, A. W., et al. 2018, AJ, 156, 195
Rucinski, S. M. 1992, AJ, 104, 1968
Siverd, R. J., Brown, T. M., Barnes, S., et al. 2018, Proc. SPIE, 10702, 107026C
Skrutskie, M. F., Cutri, R. M., Stiening, R., et al. 2006, AJ, 131, 1163
Smith, J. C., Stumpe, M. C., van Cleve, J. E., et al. 2012, PASP, 124, 1000
Stevenson, K. B., Harrington, J., Fortney, J. J., et al. 2012, ApJ, 754, 136
Stevenson, K. B., Harrington, J., Nymeyer, S., et al. 2010, Natur, 464, 1161
Szabó, R., Szabó, G. M., Dálya, G., et al. 2013, A&A, 553, A17
Tofflemire, B. M., Mathieu, R. D., & Johns-Krull, C. M. 2019, AJ, 158, 245
Tokovinin, A., Fischer, D. A., Bonati, M., et al. 2013, PASP, 125, 1336
Torres, C. a. O., Quast, G. R., da Silva, L., et al. 2006, A&A, 460, 695
van Elteren, A., Portegies Zwart, S., Pelupessy, I., Cai, M. X., & McMillan, S. L. W. 2019, A&A, 624, A120
van Eyken, J. C., Ciardi, D. R., von Braun, K., et al. 2012, ApJ, 755, 42
Vanderburg, A., Becker, J. C., Buchhave, L. A., et al. 2017, AJ, 154, 237
Vanderburg, A., Huang, C. X., Rodriguez, J. E., et al. 2019, ApJL, 881, L19

Vanderburg, A., Mann, A. W., Rizzuto, A., et al. 2018, AJ, 156, 46
Wright, E. L., Eisenhardt, P. R. M., Mainzer, A. K., et al. 2010, AJ, 140, 1868
Wright, J. T., Upadhyay, S., Marcy, G. W., et al. 2009, ApJ, 693, 1084
Wright, N. J., & Mamajek, E. E. 2018, MNRAS, 476, 381

Yu, L., Winn, J. N., Gillon, M., et al. 2015, ApJ, 812, 48
Zhou, G., Winn, J. N., Newton, E. R., et al. 2020, ApJL, 892, L21
Ziegler, C., Law, N. M., Baranec, C., et al. 2018, AJ, 156, 259
Ziegler, C., Tokovinin, A., Briceño, C., et al. 2020, AJ, 159, 19